Facile Single-Precursor Synthesis and Surface Modification of Hafnium Oxide Nanoparticles for Nanocomposite γ-Ray Scintillators

*Chao Liu, Tibor Jacob Hajagos, David Kishpaugh, Yunxia Jin, Wei Hu, Qi Chen, and Qibing Pei**

Inorganic nanoparticles/polymer nanocomposites provide a low cost, high performance alternative for gamma scintillation. However, inorganic nanoparticles used thus far suffer from either moderate atomic numbers or low band gaps, limiting the gamma stopping power and photoelectron production in these systems. Here, a highly efficient, facile single-precursor synthesis protocol is reported for hafnium oxide nanoparticles with an average diameter of 5 nm. The nanoparticle surface is further functionalized for the fabrication of highly transparent bulk-size nanocomposite monoliths (2 mm thick, transmittance at 550 nm >75%) with nanoparticle loadings up to 40 wt% (net hafnium wt% up to 28.5%). Using poly(vinyltoluene) as the matrix, 2-(4-*tert*-butylphenyl)-5-(4-biphenylyl)-1,3,4-oxadiazole and 1,4-bis(5-phenyl-2-oxazolyl)benzene as the cascade fluors, and hafnium oxide nanoparticles as the gamma sensitizer, the nanocomposite monolith of 1 cm diameter and 2 mm thickness is fabricated capable of producing a full energy photopeak for 662 keV gamma rays, with the best deconvoluted photopeak energy resolution <8%.

1. Introduction

Polymer nanocomposites, usually prepared by dispersing nanomaterials within a continuous polymeric matrix, have been widely utilized in applications such as energy harvesting,[1–3] smart materials,[4,5] and novel structural materials[6] due to their potential for multifunctionalization and property enhancement. In contrast to phase-separated macrocomposites or molecularly dissolved solutions, nanocomposites attain nanometer-scale mixing to retain certain condensed-state properties of the individual components, e.g., band structures and photoluminescent characteristics, while exhibiting other important properties characteristic of amorphous solid solutions, such as good optical transparency.[1–8] However, due to the high specific surface area and surface energy of nanomaterials, conventional mixing technique usually results in severe aggregation and phase separation within the nanocomposite, thus diminishing its uniformity and transparency.[3] Although strategies such as in situ formation of nanophase, and nanoparticle (NP) surface modification have been employed to suppress aggregation, fabrication of bulk-size nanocomposite with high loading of nanomaterials and decent transparency still poses a significant challenge.[8–12]

Spectroscopic detection of γ-rays is desirable for high energy physics study, nuclear medical imaging, and nuclear nonproliferation.[13–15] However, the detection efficiency is intrinsically limited by the high penetration power of high energy photons.[14,16,17] Other than the high-cost delicate semiconductor detectors, scintillators are the most viable solution to resolve gamma energy by, in the most ideal case, proportionally converting the radiation energy into countable visible photons.[14,16] Conventional scintillators generally fall under the categories of inorganic single-crystal scintillators and organic scintillators.[18,19] The former, typically with effective atomic numbers (effective *Z*) greater than 50, usually exhibits much better gamma stopping power than their organic counterparts (effective *Z* around 6), as the probability of depositing all energy of a gamma photon into a single fast electron (known as the photoelectric effect) is proportional to the fourth to fifth power of the material's atomic number.[14,18] In addition, the energy resolutions of inorganic single-crystal scintillators are also usually better than the organics due to higher light yield.[14] However, the demanding processes of growing large-size single crystals result in high cost for inorganic scintillators and thus hinder their widespread deployment.[16,20] Recently, high-*Z* loaded composite systems utilizing quantum dots, scintillation nanocrystals, and high-Z organometallic compounds have been proposed to increase the γ-stopping power and photoelectric cross-section for plastic scintillators.[21–29] However, reported quantum dot- and nanocrystal-polymer nanocomposites suffer from high optical loss due to aggregation and self-absorption at NP loadings higher than

C. Liu, T. J. Hajagos, D. Kishpaugh, Y. Jin, W. Hu, Dr. Q. Chen, Prof. Q. Pei
Department of Materials Science and Engineering
Henry Samueli School of Engineering and Applied Science
University of California
Los Angeles, CA 90095, USA
E-mail: qpei@seas.ucla.edu
Y. Jin
Department of Materials Science
Fudan University
220 Handan Road, Shanghai 200433, China

DOI: 10.1002/adfm.201501439

10 wt%. In addition, the moderate effective Z (around 30 to mid-50s) of these NPs limits their efficiencies in γ energy deposition. Moreover, the reported nanocomposites emit in the long-wavelength range of the visible spectrum, which limits photon detection by the commonly used commercial photomultiplier tubes (PMT) with peak sensitivity in deep blue and results in poor energy resolution.[21,22,24,26,27,30] Composites with high-Z organometallic compounds such as triphenylbismuth have demonstrated enhanced gamma stopping power. However, the poor thermal stability and relatively low band gap of triphenylbismuth (4.1 eV as compared to 4.2 eV for polyvinyltoluene (PVT), a common matrix for blue-emitting plastic scintillators) can result in substantial exciton quenching and thus a diminished light yield. In addition, molecularly dispersed high-Z compounds can also effect significant spin-orbit coupling, reducing the population of singlet excitons available to be emitted by the singlet-only emitters used in most organic scintillators.[15,23] Although a phosphorescent system comprising poly(9-vinylcarbazole) and bis[2-(4,6-difluorophenyl)pyridinato-C^2,N](picolinato)iridium(III) has recently been reported to match triphenylbismuth's band gap and triplet energy level in order to harvest both singlet and triplet and thus achieve high light yield, its application potential could still be limited due to the system's long phosphorescence decay lifetime and high cost of organo-iridium compound.[23] We have previously reported a large band gap, high-Z Gd_2O_3/polymeric matrix/fluorescent dye tertiary system for γ-ray scintillation, which is capable of producing a photoelectric peak (photopeak) with 11.4% energy resolution for 662 keV γ radiation.[8]

Figure 1 illustrates the photoelectric process in the tertiary nanocomposite system. Ideally, the high-Z NP converts all energy of an incident gamma photon into a single photoelectron. The photoelectron then undergoes energy cascade by colliding with other electrons on its path to produce a number of excitons within the matrix. Through fluorescence resonance energy transfer (FRET, which is the main energy transfer process in plastic scintillator), the excitons transfer to fluorescent dyes from which visible photons are generated.[15] The progressively decreasing band gaps going from high-Z NPs (>5 eV) to the PVT matrix (4.2 eV), and then to the dyes (<3 eV, typically at concentrations of a few percent) allow for efficient unidirectional exciton energy transfer to the dyes with little quenching. Moreover, the surface modified Gd_2O_3 (Z_{Gd} = 64) NPs can be added at a net weight percentage of about 20% without severe optical loss at thicknesses of a few mm, endowing the nanocomposites with higher stopping power as compared with the quantum dot/polymer nanocomposites in which the loading of high-Z ingredient is much lower.[8] However, the modestly high Z of Gd still limits the γ detection efficiency of this system, while the nanocomposite's green emission additionally limits its energy resolution for spectroscopic applications due to spectral mismatch with commercial PMTs.

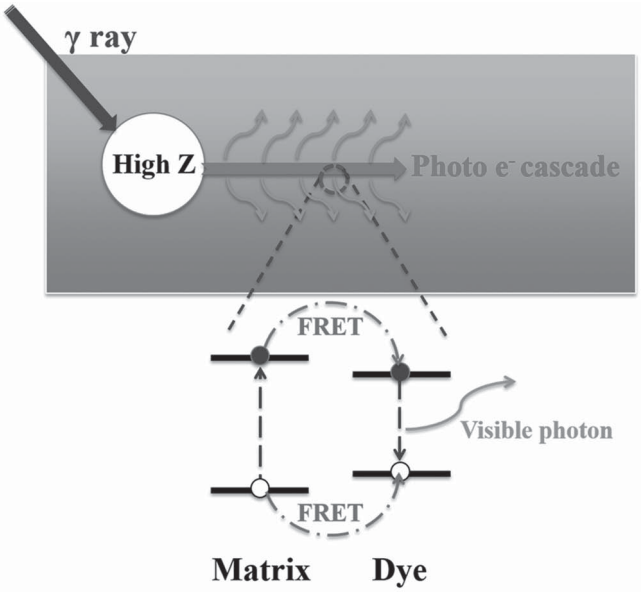

Figure 1. Gamma scintillation mechanism in a nanocomposite monolith loaded with high Z NPs.

HfO_2 has been intensively investigated in the recent years as a promising high-κ dielectric.[31] With a Z-value of 72 for Hf and reported band gaps of 5.3–6.0 eV, HfO_2 has the highest effective Z amongst all simple oxides with band gaps exceeding the 4.2 eV for PVT.[32,33] Although rare earth doped HfO_2 have also been investigated as luminescent scintillation materials, limited success was obtained due to the resulting materials' poor photophysical properties, especially the long decay time.[34,35] Thus far, the syntheses of HfO_2 NPs have been reported through a handful of methods such as hydrolysis,[36,37] solvothermal synthesis,[38,39] and nonaqueous sol–gel synthesis.[40,41] NPs produced by the first two methods tend to aggregate and precipitate in normal nonpolar solvents and are thus deemed unsuitable for fabricating uniform nanocomposites with low-polarity polymers such as PVT. While the sol–gel method can produce soluble HfO_2 NPs by condensation between $HfCl_4$ and $Hf(OCH(CH3)_2)_4$ in the presence of trioctylphospine oxide (TOPO),[40] the air- and light-sensitive nature of $Hf(OCH(CH3)_2)_4$ along with TOPO's high melting point renders the reaction protocol rather complex and therefore limits its wider applications.

Here we report a facile synthesis and surface modification protocol of HfO_2 NPs for fabricating blue-emitting nanocomposite γ-ray scintillators. Using a single precursor of $Hf(CF_3COO)_4$ in oleylamine, highly soluble HfO_2 NPs were synthesized at multigram scales with yield typically around 90%. The as-synthesized NPs were then modified with bis(2-(methacryloyloxy)ethyl) phosphate (BMEP) to endow it with surface vinyl groups, which would provide bonding between the NPs and matrix during polymerization and therefore improve dispersion uniformity of the resulting nanocomposites. Based on the commonly used matrix/primary dye/wavelength shifter recipe of PVT/2-(4-*tert*-butylphenyl)-5-(4-biphenylyl)-1,3,4-oxadiazole (PBD)/1,4-bis(5-phenyl-2-oxazolyl)benzene (POPOP),[42] we have fabricated highly transparent NP/PVT/PBD/POPOP nanocomposite scintillators by in situ polymerization of vinyltoluene (VT) solutions containing surface-modified HfO_2 NPs, PBD, and POPOP. The resulting nanocomposite monoliths exhibited high optical transparency at high NP loading. With the nanocomposite scintillator, we were able to obtain a full energy photopeak with energy resolution <8% for the 662 keV Cs-137 γ radiation.

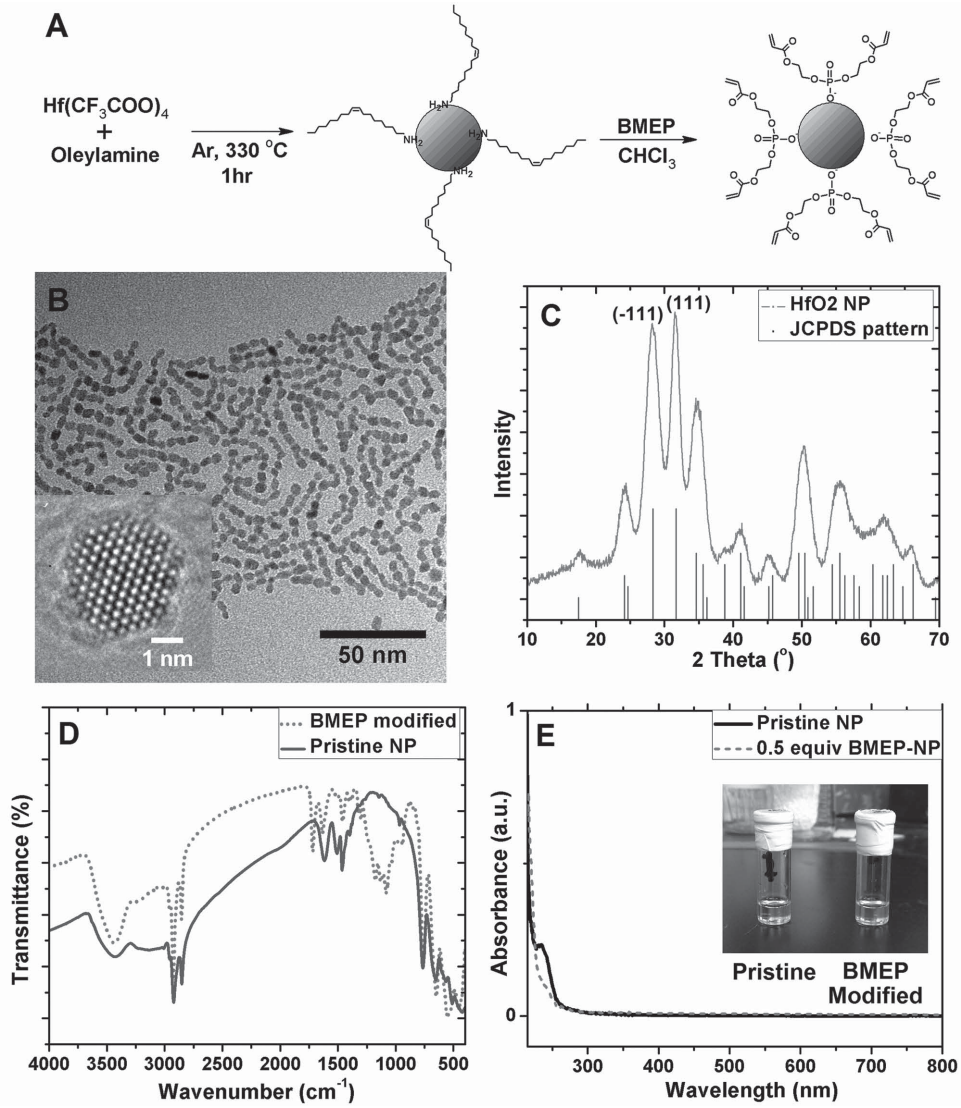

Figure 2. A) Schematic of single-precursor synthesis and surface modification of HfO_2 NPs; B) TEM image and C) powder XRD pattern of the as-synthesized HfO_2 NPs; D) FTIR spectra of HfO_2 NPs before and after BMEP exchange; and E) UV–vis absorption spectra of pristine and BMEP-exchanged HfO_2 NPs in dry tetrahydrofuran (inset: a picture of 20 wt% pristine and BMEP exchanged HfO_2 NP solutions in VT prior to curing).

2. Results and Discussion

HfO_2 NPs have been synthesized in a single-precursor reaction as schematically shown in **Figure 2**A. The precursor, $Hf(CF_3COO)_4$, was first synthesized following the protocol as previously described for $Zr(CF_3COO)_4$.[43] The similar chemical properties of Hf and Zr due to Lanthanide contraction allow these reactions to proceed in virtually the same way.[44] Owing to the high reactivity of $HfCl_4$, the reaction proceeded almost stoichiometrically, producing white $Hf(CF_3COO)_4$ with yields in excess of 96%. Structure of the as-synthesized $Hf(CF_3COO)_4$ has been confirmed by Fourier transform infrared spectroscopy (FTIR) (Figure S1, Supporting Information) and energy dispersive X-ray spectroscopy (EDX) (Figure S2, Supporting Information). The precursor is stable in air, and can be stored for months in a sealed flask without obvious signs of degradation.

The as-synthesized $Hf(CF_3COO)_4$ was then used to synthesize HfO_2 NPs capped with oleylamine in an air-free setup resembling a number of other high-temperature NP syntheses.[45,46] The reaction yield has been determined to be around 90%, indicative of the high efficiency of this single-precursor method. Transmission electron microscopy (TEM) image of the as-synthesized HfO_2 NPs shows a quite uniform size distribution around 5 nm, with most NPs having nearly round shape (Figure 2B). This size distribution is further confirmed by the dynamic light scattering results of a 45 mg mL^{-1} NP solution in toluene (Figure S3, Supporting Information). X-ray diffraction (XRD) pattern of the dried HfO_2 NPs (Figure 2C) matched well with the JCPDS profile 00–006–0318 for monoclinic HfO_2, confirming the crystallinity of HfO_2 NPs. It is well known that nanosized crystals can cause line broadening in the XRD pattern, and the Scherrer equation can be used to calculate crystallite size from line broadening

$$\tau = \frac{K\lambda}{\beta \cos\theta} \quad (1)$$

where τ, K, λ, β, and θ are crystallite size, shape factor (typically around 0.9), wavelength of the X-ray (0.154 nm for Cu Kα1), full-width-half-maximum (FWHM) of the broadened line, and the Bragg angle for the diffraction peak, respectively. After stripping the Cu Kα2 signal from the spectrum and accounting for the instrumental broadening of 0.07°, crystallite sizes were calculated to be 6.0 and 5.3 nm for the (–111) and (111) planes, respectively, showing a close match to results obtained from the TEM images.

To determine the mechanism behind HfO_2 NP formation, a series of synthetic tests were performed under various concentrations of $Hf(CF_3COO)_4$. As shown in Figure S4, Supporting Information, the product HfO_2 NPs show no obvious crystallinity differences at $Hf(CF_3COO)_4$/oleylamine molar ratios of 1:40 and 1:20, whereas the crystallinity decreased slightly for the 1:160 reaction, most likely due to an insufficient supply of precursors. However, for the $Hf(CF_3COO)_4$/oleylamine = 1:20 experiment, the viscosity of reaction mixture drastically increased at around 290 °C, leading to a gel-like appearance. Moreover, upon further increasing the temperature to 330 °C, the mixture eventually achieved the characteristic colorless, low-viscosity solution typical of the reaction. This observation indicates that the reaction may follow a sol-gel process where oleylamine first attacks the trifluoroacetate ligand to form Hf—OH, followed by condensation to form HfO_2 NPs (Figure S5, Supporting Information). The initial increase of viscosity at 290 °C could be ascribed to the formation of partially condensed loose networks of Hf—O—Hf, which is incapable of dissolving in limited amounts of oleylamine, and merely swells to form a gel. Further increasing the degree of condensation led to the formation of suspended dense NPs, thus reducing the viscosity. This mechanism can be further corroborated by the failed reactions using oleic acid instead of oleylamine. Since the formation of Hf—OH was prevented in the first place by the acidic environment in oleic acid, no crystals could be obtained, but a yellow oil was produced.

The as-synthesized NPs were assumed to be coated by a layer of oleylamine due to their excellent solubility in low-polarity solvents, which was confirmed by the FTIR spectrum of unmodified HfO_2 NPs shown in Figure 2D. The peaks at 1620 and 3001 cm^{-1} can be ascribed to the C=C and vinyl C—H vibrations for oleylamine, respectively.[47] The N—H bending vibrations at 1514 cm^{-1} and stretching band at around 3200 cm^{-1} also indicate the presence of oleylamine, whereas the lack of peaks at 1000–1250 cm^{-1} excludes the possibility of remaining carboxylic acid bonding to the surface.

The oleylamine ligands bound on NP surface have unsaturated C=C bonds. These vinyl groups are relatively unreactive and cannot be readily copolymerized with vinyl monomers such as VT to provide bonding between the NPs and a PVT matrix. Therefore, direct curing of VT solutions containing oleylamine-capped NPs resulted in severe phase separations and thus transmittance loss due to exclusion of NPs during polymerization. Since the visible photons generated within the scintillator monolith need to transmit through the bulk and be detected by PMT, it is crucial to reduce phase separation and transmittance loss to improve the detection efficiency. BMEP was then used to introduce methacrylate monomer groups onto the NP surface to promote copolymerization with the matrix.[8] The suitable reactivity ratios (ratios between possibilities of one monomer reacting to itself versus to the other in a binary copolymerizing system) of 0.52 and 0.46 for styrene and methyl methacrylate, respectively, promise a good chance of copolymerization between VT and the methacrylate-containing BMEP, rendering BMEP a suitable surface modifier.[48] Strong bonding between hafnium and phosphate guarantees a strong anchoring of BMEP surface layer, while the acid-inert nature of bulk HfO_2 assured an intact crystallinity of HfO_2 NPs after ligand exchange.[44] Figure 2D compares the FTIR spectra of pristine HfO_2 NPs and fully BMEP-exchanged HfO_2 NPs. The previously described spectral features of oleylamine coated HfO_2 NPs disappeared after BMEP exchange. Instead, a set of new peaks appeared at 1716, 1633, 1173, 1114, and 1078 cm^{-1}, corresponding to the C=O, C=C, C—O, and P—O stretching absorptions.[8] These obvious changes in spectral features confirm the effectiveness of surface modification using BMEP.

Due to the strong bonding between hafnium and phosphate, the reaction between BMEP and HfO_2 NPs should be able to proceed almost stoichiometrically.[44] This has been confirmed by the thermogravimetric analysis (TGA) and FTIR results of pristine and BMEP-modified HfO_2 NPs at different BMEP-exchange ratios (Figure S6 and S7, Supporting Information). It should be noted that using an excess amount of BMEP would not result in more BMEP attachment than that limited by the available surface states, indicating a good stability of HfO_2 NPs against corrosion by acids, which is further confirmed by the unchanged XRD pattern after BMEP modification (Figure S8, Supporting Information). Therefore, the degree of surface modification can be controlled by varying the amount of BMEP used. The solubility of BMEP-exchanged NPs in VT was found to decrease with an increasing degree of BMEP exchange, likely due to the higher polarity of BMEP than oleylamine. However, excessively low percentages of BMEP exchange would result in insufficient bonding between the matrix and NP and thus lead to phase segregation and transmittance loss. HfO_2 NPs exchanged with 50% BMEP (1:1 molar ratio of oleylamine/BMEP on the modified NPs) were found to be optimal in balancing between the solubility and surface monomer density; this percentage would be used in all nanocomposite fabrications thereafter.

As stated above, an important reason for choosing HfO_2 as the high-Z component is that its large band gap prohibits matrix-to-NP exciton energy transfer, thus avoiding excess exciton quenching. To confirm HfO_2's large band gap, optical absorbance of both pristine and BMEP-modified HfO_2 NPs were tested using UV–vis spectroscopy. Due to the decreased solubility of BMEP-modified NP in hexane, distilled tetrahydrofuran (no optical absorption at >210 nm) was used to dissolve both samples for the spectroscopic measurement. Figure 2E shows the absorption spectra of these NPs at concentration of 0.5 mg mL^{-1}. The absorption peak at 240 nm for pristine NPs is consistent with the reported absorption for oleylamine,[49] whereas the absorption onset at 230 nm for BMEP-modified NPs matched well with the measurement of a 0.05 mg mL^{-1} BMEP solution (Figure S9, Supporting Information). No other

strong absorption was observed above 215 nm for both NPs, indicating a band gap of at least 5.7 eV, which would be more than sufficient to prevent exciton transfer from PVT to NPs. The 50%-BMEP-modified HfO_2 NPs showed no obvious degradation of solubility in VT compared to the pristine NPs, as indicated by the colorless transparent solutions of 20 wt% pristine and modified NPs in VT (see inset of Figure 2E).

Using the highly soluble BMEP-modified HfO_2 NPs, NP/PVT/PBD/POPOP nanocomposite monoliths were fabricated using a thermally initiated bulk polymerization process.[8] **Figure 3**A shows the TGA curve of a 20 wt% NP composite tested in air (all NP concentrations are wt% including the organic ligand content henceforth, if not specified). The remnant of 16.5% matches well with the estimation of 20% * (1–0.16) = 16.8%, where 20% is the initial NP loading, with the organic ligand content of NPs being 16% as determined previously. The NP nanocomposites displayed high transparency after curing. Figure 3B shows the transmittance curves and photos of a 2 mm 20% NP nanocomposite along with its NP-free counterpart. No obvious transparency differences are evident from visual inspection. On the spectra, the sharp drop at 400 nm is due to POPOP absorption. The 20% NP nanocomposite showed a slightly lower transmittance compared to its NP-free counterparts above 400 nm. Compared with the relatively flat curve for NP-free composite ($T_{550\ nm}$ = 90.9%, $T_{415\ nm}$ = 88.6%), transmittance of the NP nanocomposite degraded faster with decreasing wavelength ($T_{550\ nm}$ = 83.7%, $T_{415\ nm}$ = 72.9%). This can be attributed to an intensified Rayleigh scattering induced by the presence of NPs, as the transmittance loss due to scattering is strongly wavelength dependent ($\propto \exp(-C/\lambda^{-4})$, where C is a material property related constant).[9,12] Moreover, it is suspected that the NPs could still aggregate, but to a smaller extent, during polymerization, since the gradual formation of polymer network would still lead to some degree of NP exclusion. To confirm this, TEM images were obtained on a thin-film sample (about 50 nm thick) of the 20% NP nanocomposite prepared using focused ion beam. As shown in Figure 3C, although the NP dispersion was fairly uniform within the polymer matrix, some NPs aggregate into clusters of about 20 to 30 nm sizes, which could be the major source of scattering-induced transmittance loss. It should be noted that the thin film of 50 nm could contain several layers of NPs, which might lead to some degree of overestimation on the aggregation effect due to the possibility of overlapped NPs in the TEM image.

As mentioned before, HfO_2 NPs in the nanocomposite will serve as high-Z component to convert an incident γ photon into a single photoelectron with all energy in the original γ photon. The high-energy photoelectron then undergoes energy cascade within the PVT matrix by colliding with other electrons on its decay path, where a number of excitons are produced in proportion to the photoelectron energy. Through FRET, these excitons will migrate to the PBD dye sites and be converted into visible photons for detection. This energy transfer process needs to be highly efficient to maximize light yield (number of photons generated per MeV of γ energy), since the fluorescence quantum efficiency of PVT is very low. In addition to the primary dye of PBD, POPOP is used as a wavelength shifter at very low concentration (0.01%) to further shift PBD's emission

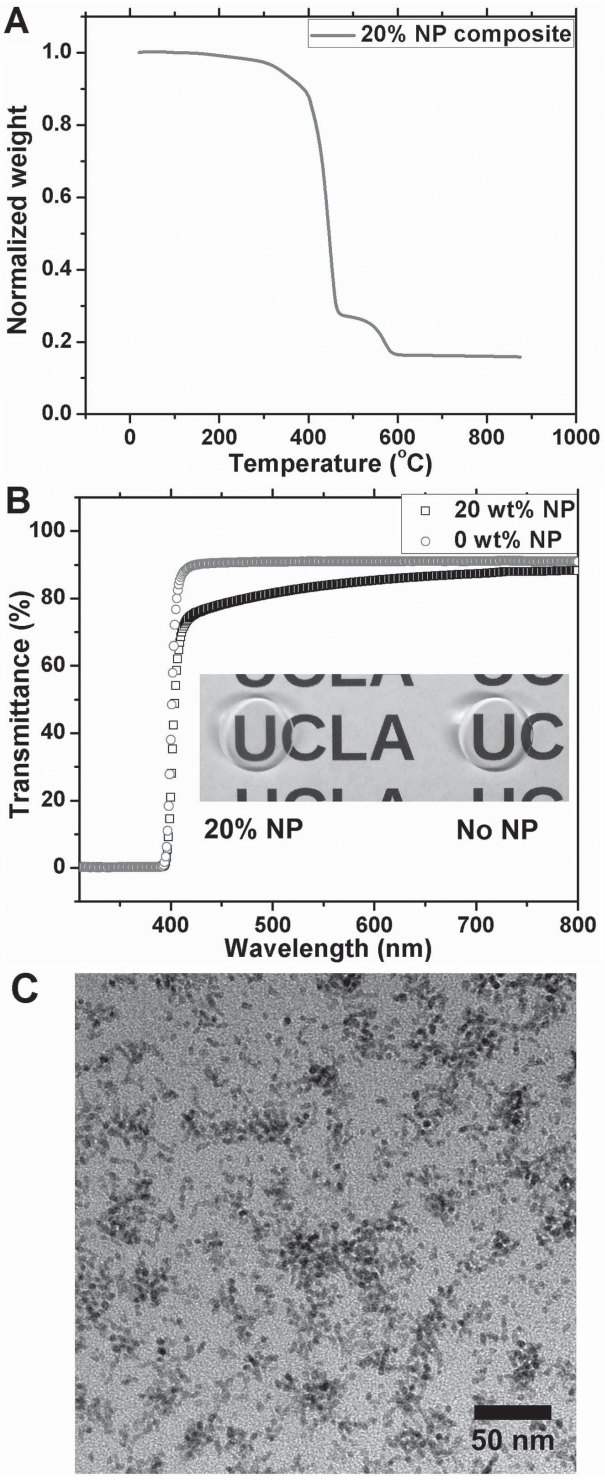

Figure 3. A) TGA curve of a 20% NP/PVT/PBD/POPOP composite monolith; B) UV–vis transmittance curves and pictures of 2 mm thick NP-free and 20% NP/PVT/PBD/POPOP composite monoliths; and C) TEM image of a FIB-etched thin film of 20% NP composite.

in order to reduce self-absorption.[15,18,42] The combination of PVT/2% PBD/0.01% POPOP has been widely reported to have a good light yield and therefore was used for the nanocomposite scintillators in this work.[18,42]

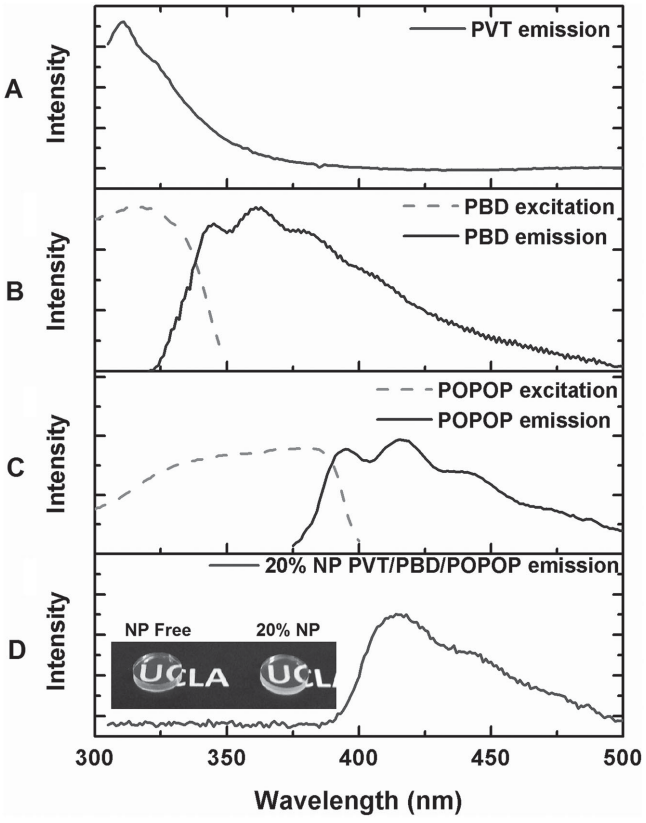

Figure 4. A) Photoluminescence spectra of pure PVT monolith, B) dilute PBD/$CHCl_3$ solution, C) dilute POPOP/$CHCl_3$ solution, and D) 20% NP/PVT/PBD/POPOP nanocomposite monolith. Inset photograph in D) shows PVT/PBD/POPOP monoliths (2 mm thick by 1 cm diameter) containing zero (left) and 20% NPs (right) under 256 nm UV illumination. The excitation wavelengths used for taking emission spectra were 298, 311, 365, and 298 nm for PVT, PBD, POPOP, and the 20% NP nanocomposite, respectively. The excitation spectra were obtained by measuring the emission intensity at 365 and 415 nm for PBD and POPOP, respectively.

To confirm the aforementioned energy transfer processes, a photophysics study was performed using photoluminescence spectroscopy. **Figure 4** shows the photoluminescence spectra of a monolith of neat PVT, dilute solutions of PBD and POPOP, and a 20% NP/PVT/PBD/POPOP nanocomposite monolith. The emission maximum of PVT at 311 nm matches the excitation of PBD, while PBD's emission maximum at 365 nm overlapped nicely with the excitation of POPOP. These well-matched emission/excitation pairs promise efficient FRET transfers from PVT to PBD and finally via radiative transfer to POPOP. As shown in Figure 4D, the 20% NP/PVT/2% PBD/0.01% POPOP nanocomposite exhibited only POPOP emission at the PVT excitation wavelength of 298 nm, confirming an efficient energy transfer process. The inset of Figure 4D shows the picture of a NP-free and a 20% NP/PVT/PBD/POPOP nanocomposite monoliths under 256 nm UV illuminations, where no discernable differences in the emission color and intensity could be observed.

Gamma responses of the blue-emitting nanocomposites were characterized using a homebuilt gamma pulse height analysis system. Pulse height spectra were first obtained on three samples including an NP-free PVT/PBD/POPOP nanocomposite, a 20% NP PVT/PBD/POPOP nanocomposite, and an Eljen-212 commercial plastic scintillator polished to the same size as the nanocomposite monoliths. **Figure 5**A shows the pulse height spectra obtained for these three samples. The appearance of a Compton edge is due to the Compton backscattering of gamma photons, and its position depends solely on the energy of the incident gamma photon.[14] For 662 keV γ, the Compton edge corresponds to a deposited energy of 478 keV. Therefore, using the channel number of Compton edge (typically chosen as the inflection point on the slope), we can compare the γ light yields of these three monoliths. The channel numbers for the Compton edges of Eljen-212, NP-free composite, and 20% NP nanocomposite were 1110, 1100, and 840, respectively. With the light yield of Eljen-212 being 10000 photons/MeV, the light yields of NP-free and 20% NP nanocomposites would be 9900 and 7600 photons/MeV, respectively. The similar light yield of PVT/PBD/POPOP with Eljen-212 is consistent with previous reports.[18,42] However, the decrease in light yield with NP inclusion may not be due to exciton quenching as reported in literatures using organometallics as the high-Z component, since the NPs possess a much larger band gap than the organic components and therefore cannot capture and trap the low energy excitons and photons from the organics.[23,50] Nevertheless, a plausible case might be that the energy deposited within HfO_2 during photoelectron cascade could be trapped and dissipated without producing photons, leading to degradation in the composite's overall photon generation power and thus light yield. In addition, a more obvious reason behind light yield deterioration is the loss of transmittance due to scattering induced by NPs, which affects the efficiency of photons generated inside the monolith being out-coupled to the PMT.

In order to investigate these causes of light yield deterioration, three sets of experiments have been performed. The first two sets used 10% NP and 20% NP PVT/PBD/POPOP monoliths, respectively, at different thicknesses (2, 4, and 6 mm) to determine the effect of transmittance on light yield. In the third set, a series of 2 mm thick monoliths with 0% to 40% NP loadings were tested, where the combined effects of transmittance loss and energy trapping in NPs on light yield could be observed. Relative light yields of the samples were obtained by dividing their Compton edge channel numbers by that of the 2 mm thick PVT/PBD/POPOP monolith. To characterize the light out-coupling ability of monoliths, the transmittance at 415 nm was chosen as the figure of merit, since the emission maxima of nanocomposite monoliths have all been located at this wavelength as shown in Figure 4. Figure 5B shows the relative light yields and transmittances at 415 nm obtained for these monoliths (original data shown in Figure S10–S12, Supporting Information). In each curve for the 10% and 20% NP monoliths, the relative light yield showed a somewhat linear dependence on transmittance, consistent with the as-proposed effect of transmittance, or light out-coupling, on light yield. However, for these two curves, in addition to the curve for 2 mm thick monoliths with different NP loadings, large discrepancies in relative light yields were found amongst samples with the same transmittance but different NP%, indicating a significant influence from the NPs themselves in addition to the transmittance loss.

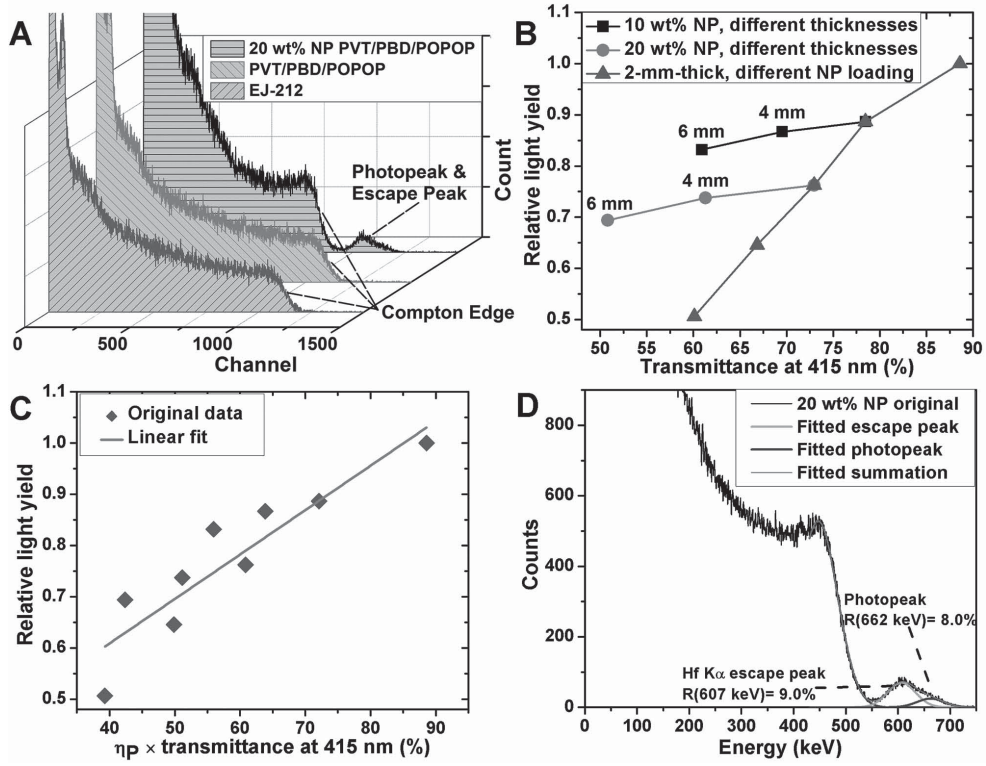

Figure 5. A) Pulse height spectra obtained for monoliths of PVT/PBD/POPOP, 20% NP/PVT/PBD/POPOP, and the standard Eljen-212 scintillator; B) relative light yield vs. transmittance at 415 nm for 10% and 20% NP composites with different thicknesses (2, 4, and 6 mm), and for 2 mm thick monoliths with 0% to 40% NP with 10% increment; C) relative light yield replotted and linearly fitted as a function of the product of relative photon generation power (η_P) and transmittance at 415 nm for data points in (B); and D) energy correlated pulse height spectrum and fitted curve for a 2 mm thick 20% NP PVT/PBD/POPOP monolith.

As mentioned above, the NP's large band gap excludes possibilities of quenching excitons from organics and absorbing photons emitted by fluorescent dyes. A plausible mechanism behind this NP-induced extra light yield deterioration is the loss of energy trapped in NPs during fast electron cascade, since the NPs are not fluorescent and cannot transfer the deposited energy into the organic matrix via FRET. For a quantitative consideration, this part of trapped energy should be proportional to the volume percentage of NPs multiplied by their fast electron stopping power. (Note: this is still a somewhat simplified model, a more detailed discussion has been provided by Bulin et al.)[51] The fast electron stopping power in matter is directly proportional to that matter's electron density because a fast electron goes through energy cascade via collisions with electrons in the matter sitting in its tortuous pathway. The organic components, PVT, PBD, and POPOP, have similar atomic compositions and thus almost identical electron densities. HfO_2 NPs, on the other hand, have a much higher electron density than the organics and thus a greater stopping power for fast electron.

Based on the statement above, the percentage of energy (E_i) deposited in component i in the nanocomposite can be expressed using the normalized product of stopping power ($-dE/dx$) and volume percentage (V)

$$E_i = \frac{V_i\left(-\frac{dE}{dx}\right)_i}{\sum_i V_i\left(-\frac{dE}{dx}\right)_i} \quad (2)$$

The relationship between fast electron stopping power and the electron density of matter has been given by Bethe[14]

$$-\frac{dE}{dx} \propto \frac{Z\times\rho}{A} \quad (3)$$

where Z, ρ, and A are the atomic number, volumetric mass density and relative atomic mass of the matter, respectively. Assuming all fast electron energy deposited in NPs and NP-bound ligands (which lack conjugated π-electrons for hosting excitons) dissipates without producing photons, and the energy deposited in organic matrix (including dyes) is used to generate photons, the relative photon generation power (η_P) is then directly proportional to the percentage of energy deposited within the organic matrix (E_M) and can be expressed as follows using Equations (2) and (3)

$$\eta \propto E_M = \frac{V_M \frac{Z_M \times \rho_M}{A_M}}{V_M \frac{Z_M \times \rho_M}{A_M} + V_{NP} \frac{Z_{NP} \times \rho_{NP}}{A_{NP}} + V_L \frac{Z_L \times \rho_L}{A_L}} \quad (4)$$

where the subscripts M, NP, and L denote matrix, NPs and ligands, respectively. For each component, the volume percentage was calculated using wt% and density, whereas Z and A were taken as the total Z and relative molecular mass, respectively, e.g., $Z_{NP} = 88$, $A_{NP} = 210.5$ for HfO_2. From this expression, it is clear that although the volume percentage of HfO_2 NPs is small compared with the organics, the amount of energy trapped during the fast electron cascades can still be significant due to the NPs much higher electron density.

The overall light yield determined by PMT depends not only on the generation but also out-coupling of the photons to the photodetector. It is thus proportional to the product of transmittance and relative photon generation power η_P. Figure 5C plots the relative light yield against the product of transmittance at 415 nm and calculated η_P for the data points shown in Figure 5B. A greatly improved linearity is seen, which is indicative of a good agreement between experimental results and the proposed combined effects of photon generation and out-coupling on light yield. It should be noted that the usage of transmittance at 415 nm as the light out-coupling power would be a great underestimation of the true value, which should have contributed to the degradation of linearity in the light yield relationship shown in Figure 5C. This is due to the fact that most scattered photons are lost and not being detected by the detectors in an UV–vis test, whereas for the scintillator wrapped by a set of Teflon reflectors, a substantial fraction of scattered photons can eventually reach the PMT after multiple scattering and reflections. Since the large band gap NPs do not absorb low energy photons, the decreased light out-coupling power should only be ascribed to an increased self-absorption within the matrix due to multiscattering induced extension of light path. Accounting for this effect of photon scattering requires random-walk simulations with geometrical considerations, which would be out of the scope of discussion for this paper; however, with a more accurately represented light out-coupling term, a greatly improved linear relationship between light yield and the product of light out-coupling power with η_P should be obtainable, which should also intercept with the axes at origin. Although the NP nanocomposites showed some decay in light yield due to scattering-induced transmittance loss and energy trapping in the NPs, the addition of HfO_2 NPs produced a full energy photoelectron peak in the gamma pulse height spectrum as shown in Figure 5A (also Figure S10–S12 for all other nanocomposites). The presence of this peak is due to the drastically increased possibility of photoelectric process in the NP-containing nanocomposites, which produces photoelectrons with full 662 keV energy from gamma photons. Since the probability of photoelectric effect is roughly proportional to the fourth to fifth power of Z, the likelihood of producing a full energy photoelectron in Hf (Z = 72) is about 12^4 to 12^5 times of that for carbon (Z = 6). As a result, although no photopeaks can be clearly resolved with typical organic scintillators, the addition of HfO_2 endows it with the ability to show full energy peaks of gamma rays, and therefore promises gamma spectroscopic applications. To further study the gamma energy resolving power of this nanocomposite, we have obtained another pulse height spectrum with a 2 mm thick 20% NP composite using an acquisition time of 4 h. The longer acquisition time improves signal-to-noise ratio and thus improves the statistical reliability. As shown in Figure 5D, a full energy peak consisting of a main peak at 607 keV and a shoulder peak at 662 keV was observed. Positions of these peaks are in good agreement with those of a true photopeak (662 keV) and a Hf Kα escape peak (662 – 55 = 607 keV). The high-Z Kα escape peak have been reported in a number of publications using small trial-size scintillators and should disappear at larger scintillator sizes due to diminished possibilities of the high-Z Kα X-ray escaping the scintillator.[14,23] The photopeak and Hf Kα escape peak were subsequently fitted into two Gaussian peaks with energy resolutions (defined as FWHM/peak energy) of 8.0% and 9.0%, respectively (R^2 = 0.995, Figure 5D). Pulse height spectrum of a 10% NP nanocomposite monolith was also measured and shown in Figure S13, Supporting Information, with deconvoluted photopeak and escape peak resolutions of 5.8% and 8.3%, respectively. It should be noted that the fitted 5.8% photopeak resolution for 10% NP nanocomposite is likely an over-optimistic value (resolution around 7.5% would be more plausible) due to fitting errors induced by weak photopeak intensity, since photon statistics dictate that the resolution of photopeak should only be slightly better than the escape.[14] As a more conservative note, fitting the full energy peak as a whole also gives resolutions of 9.6% and 10.8% for the 10% and 20% NP nanocomposites, respectively (Figure S14, Supporting Information). These results compare favorably with the previous reported value of 11.4% obtained using 31% Gd_2O_3 nanocomposites (net Gd_2O_3 NP loading around 20%).[8] One contribution to this improvement is the difference in PMT spectral sensitivity: the PMT is two times more sensitive to the present nanocomposite's deep blue emission than the green emission from previous Gd_2O_3 nanocomposite.[14,15] The greater PMT sensitivity results in a higher apparent light yield (photons detected by the PMT) and thus better resolution for the blue scintillator, since the resolution is inversely proportional to the square root of light yield.[14,15]

The photoelectric cross-section of Hf is about 1.6–1.8 times of that of Gd (Z = 64); therefore, the photoelectric efficiency for 10% HfO_2 NP composite (net HfO_2 loading around 8.4%) is not much lower than that of the 31% Gd_2O_3 NP composite (net Gd_2O_3 NP loading around 20%), whereas the 20% monolith (net HfO_2 loading around 16.8%) has an even higher photoelectric efficiency than the 31% Gd_2O_3 composite. This relatively high photoelectric probability at lower NP% is beneficial, because both scattering and energy trapping increase with NP% and would thus deteriorate light yield. This is particularly important for the fabrication of nanocomposite monoliths sufficiently large for gamma spectroscopy. As the scintillator size increases, the X-ray escape peak would eventually disappear due to recapture of the escaping Hf Kα X-ray photon. Since the attenuation depth for a 50 keV X-ray photon is typically around a few cm in water, the disappearance of escape peak should be expected at sizes of several cubic inches for a low NP% composite monolith.

3. Conclusion

In summary, HfO_2 NPs with fairly uniform size distribution and excellent solubility in low-polarity solvent have been synthesized via a facile single-precursor method at high yield. The oleylamine ligand on NP surface can be replaced by BMEP to introduce polymerizable functional groups. Bulk polymerization of the modified NPs dissolved in VT has produced bulk monoliths that remained transparent at NP loading as high as 40 wt%. Blue-emitting nanocomposite γ-ray scintillation monoliths have been synthesized, and a 2 mm thick sample comprising up to 20 wt% NPs, 2% PBD, and 0.01% POPOP produced a deconvoluted photopeak with energy resolution ≤8% for 662 keV Cs-137 γ radiation. The synthesis has high yield, and should be scalable to larger-size monoliths. However, the gamma light yield and photopeak resolution do not seem to improve with larger monoliths or higher loading, which may be attributed to aggravated light scattering and energy trapping during photoelectron cascade. Further work is underway to overcome the light scattering issue, subdue the escape peak, and improve the photopeak resolution. In addition to the gamma scintillator application, with the facile syntheses and surface modification protocol developed in this paper, the highly soluble, chemically inert, high-refractive-index HfO_2 NPs should also find applications such as in composite high-κ dielectrics and biocompatible contrast agents in X-ray computed tomography.

4. Experimental Section

Materials: Hafnium(IV) tetrachloride (99%, 80 mesh) and 1,1-di-(*tert*-butylperoxy)-3,3,5-trimethylcyclohexane (DTTMC, 75% solution in aromatic free mineral spirit) were purchased from Acros Organics. Oleylamine (OAm, Technical grade, 70%), bis(2-(methacryloyloxy)-ethyl) phosphate (BMEP), methylstyrene (commonly referred to as vinyltoluene, VT, 99%), 2-(4-*tert*-butylphenyl)-5-(4-biphenylyl)-1,3,4-oxadiazole (PBD, 99%), and 1,4-bis(5-phenyl-2-oxazolyl)benzene (POPOP) were purchased from Sigma-Aldrich. Trifluoroacetic acid (99%) was purchased from EMD. Excluding chloroform (HPLC grade), all other solvents used were of ACS grade. Tetrahydrofuran was distilled from sodium benzylphenone ketyl prior to use. VT was purified by a mini column packed with inhibitor removers to remove *tert*-butylcatechol before use. An Eljen-212 general-purpose plastic scintillator was obtained from Eljen Technology and was polished into a disk with dimensions 10 mm in diameter and 2 mm thickness to serve as the standard for scintillation measurements. All other materials were used as received.

Synthesis and Fabrication: $Hf(CF_3COO)_4$ was synthesized following the protocol for $Zr(CF_3COO)_4$ previously described by Sartori and Weidenbruch.[43] Trifluoroacetic acid (50.0 mL, ≈650 mmol) was slowly added to $HfCl_4$ (30 mmol, 9.60 g) under stirring. The mixture was stirred at 40 °C for 5 h and then dried by rotary evaporation and high vacuum to obtain $Hf(CF_3COO)_4$ in the white solid form. Typical yield of the reaction is >96%. The high-temperature synthesis of HfO_2 NPs from $Hf(CF_3COO)_4$ was carried out under inert gas protection. In a typical reaction, $Hf(CF_3COO)_4$ (4 mmol, 2.52 g) was mixed with OAm (52.6 mL, ≈160 mmol) and stirred under vacuum for 30 min at 110 °C. The resulting transparent solution was then heated to 330 °C for 1 h under Ar, after which the nearly-colorless transparent solution was cooled to room temperature. White HfO_2 NPs were flocculated by adding 150 mL acetone, collected by centrifugation, and washed (redissolving and flocculating with toluene and ethanol, respectively) three times. Finally, the NPs were dissolved in 20 mL toluene to form a stable colorless stock solution of around 45 mg mL^{-1} (weight concentration includes surface ligand), corresponding to a yield of about 90% after accounting for the 82% net inorganic weight as determined through TGA. Surface modification of the NPs was carried out by admixing the as-prepared HfO_2 with a predetermined amount of BMEP in chloroform and stirring overnight. The resulting solution was first concentrated using rotary evaporation, then washed three times with hexane and acetone following the similar redissoving-flocculating procedure described above. The washed NPs were dissolved in a nanocomposite precursor solution composed of 2 wt% PBD, 0.01 wt% POPOP and 1 vol% DTTMC in purified VT. The clear solution was placed in 10 mm diameter glass vials and cured (100 °C, 24 h) in a nitrogen protected glove box. After curing, the resulting monoliths were removed from the glass vials and polished for further characterizations.

Characterization: Transmission electron microscopy was performed on a FEI T12 Quick CryoEM and CryoET microscope operated at 120 keV. High resolution TEM images were taken on a FEI Titan S/TEM operated at 300 keV. The nanocomposite thin-film TEM samples were prepared by focused ion beam etching of the monolith using a FEI Nova 600 SEM/FIB system. Powder X-ray diffraction data was obtained using a Panalytical X'Pert Pro X-ray powder diffractometer with Cu Kα radiation. Fourier transform infrared spectra were obtained using a Jasco 420 FTIR spectrophotometer with KBr pelletized samples. Dynamic light scattering was performed on a Coulter Beckman N4 Plus Dynamic Light Scattering Analyzer. UV–vis tests were carried out on a Shimadzu UV-1700 spectrophotometer. Homemade masks were applied to reduce the light path variations for monolith transmittance tests. Photoluminescence spectra were obtained with a PTI QuantaMaster 30 spectrofluorometer. Thermogravimetric analysis was performed on a Perkin Elmer Diamond Thermogravimetric/Differential Thermal Analyzer. The sample was first stabilized at 100 °C for 10 min to remove residue solvents and water before being heated to 850 °C in air at a ramping rate of 15 °C min^{-1}, after which it was kept at 850 °C for another 10 min to ensure complete decomposition. Energy dispersive X-ray spectroscopy was performed on a FEI Nova Nano 230 scanning electron microscope operated at 10 keV. The EDX samples were first dispersed in corresponding solvents and drop-casted onto Cu tape, followed by high-vacuum drying.

Gamma Pulse Height Analysis of the Monoliths: Gamma pulse height analysis was performed with a home-built system in a dark box as shown in Scheme S1, Supporting Information, where a Cs-137 source (662 keV characteristic γ energy) of 4.68 μCi activity (1.7×10^5 disintegrations/second) was placed right in front of the nanocomposite monolith coupled to a Hamamatsu R878 PMT using optical grease. A set of customized Teflon reflector ring and back-reflector disk was used to optimize the light collection by PMT and to exclude the influence of concomitantly emitted β rays from the Cs source. The PMT was equilibrated for 30 min after sealing the dark box. Typical acquisition live time was set to 1 h unless specified otherwise. The signal was read out by a Canberra multichannel analyzer with rise and flat top times set to 1 and 0.5 μs, respectively.

Supporting Information

Supporting Information is available from the Wiley Online Library or from the author.

Acknowledgements

The authors are indebted to Dr. Nerine Cherepy and Dr. Stephen Payne of the Lawrence Livermore National Laboratory, and Prof. Arion Chatziioannou of the UCLA Department of Molecular & Medical Pharmacology for invaluable discussions on scintillation photophysics and measurement techniques. This work was financially supported in part by the Defense Threat Reduction Agency (HDTRA1–14–1–0032).

The scintillation instrumentation was funded by National Science Foundation (ECCS - 1348403). The University of California Lab Fees Research Program (UCOP Grant No. 12-LR-237678) is acknowledged for the initial exploratory investigation. The authors thank Dr. Noah Bodzin at the UCLA Nanoelectronics Research Facility for his kind help in FIB sample preparation. C.L. is grateful for the valuable discussions and comments from Dustin Chen, Yongjia Li, and Enbo Zhu. The authors acknowledge the use of instruments at the Electron Imaging Center for NanoMachines supported by NIH (1S10RR23057 to ZHZ) and CNSI at UCLA.

Received: April 10, 2015
Revised: May 4, 2015
Published online: June 12, 2015

[1] A. S. Aricò, P. Bruce, B. Scrosati, J. Tarascon, W. Van Schalkwijk, *Nat. Mater.* **2005**, *4*, 366.
[2] Z. Yu, L. Li, Q. Zhang, W. Hu, Q. Pei, *Adv. Mater.* **2011**, *23*, 4453.
[3] A. C. Balazs, T. Emrick, T. P. Russell, *Science* **2006**, *314*, 1107.
[4] H. Koerner, G. Price, N. A. Pearce, M. Alexander, R. A. Vaia, *Nat. Mater.* **2004**, *3*, 115.
[5] W. Hu, S. N. Zhang, X. Niu, C. Liu, Q. Pei, *J. Mater. Chem. C* **2014**, *2*, 1658.
[6] S. Stankovich, D. A. Dikin, G. H. B. Dommett, K. M. Kohlhaas, E. J. Zimney, E. A. Stach, R. D. Piner, S. T. Nguyen, R. S. Ruoff, *Nature* **2006**, *442*, 282.
[7] J. Liang, L. Li, K. Tong, Z. Ren, W. Hu, X. Niu, Y. Chen, Q. Pei, *ACS Nano* **2014**, *8*, 1590.
[8] W. Cai, Q. Chen, N. Cherepy, A. Dooraghi, D. Kishpaugh, A. Chatziioannou, S. Payne, W. Xiang, Q. Pei, *J. Mater. Chem. C* **2013**, *1*, 1970.
[9] B. M. Novak, *Adv. Mater.* **1993**, *5*, 422.
[10] Y. Li, P. Tao, A. Viswanath, B. C. Benicewicz, L. S. Schadler, *Langmuir* **2013**, *29*, 1211.
[11] S. Lee, H.-J. Shin, S.-M. Yoon, D. K. Yi, J.-Y. Choi, U. Paik, *J. Mater. Chem.* **2008**, *18*, 1751.
[12] C. Lü, B. Yang, *J. Mater. Chem.* **2009**, *19*, 2884.
[13] C. W. E. Van Eijk, *Phys. Med. Biol.* **2002**, *47*, R85.
[14] G. F. Knoll, *Radiation Detection and Measurement*, John Wiley & Sons, Hoboken, NJ **2010**.
[15] J. B. Birks, *The Theory and Practice of Scintillation Counting*, Pergamon, Oxford, England **1964**.
[16] B. D. Milbrath, A. J. Peurrung, M. Bliss, W. J. Weber, *J. Mater. Res.* **2011**, *23*, 2561.
[17] A. Owens, *J. Synchrotron Radiat.* **2006**, *13*, 143.
[18] V. N. Salimgareeva, S. V Kolesov, *Instrum. Exp. Technol.* **2005**, *48*, 273.
[19] G. Blasse, *Chem. Mater.* **1994**, *6*, 1465.
[20] S. E. Derenzo, W. W. Moses, J. L. Cahoon, R. C. C. Perera, J. E. Litton, *IEEE Trans. Nucl. Sci.* **1990**, *37*, 203.
[21] S. E. Létant, T.-F. Wang, *Nano Lett.* **2006**, *6*, 2877.
[22] I. H. Campbell, B. K. Crone, *Adv. Mater.* **2006**, *18*, 77.
[23] B. L. Rupert, N. J. Cherepy, B. W. Sturm, R. D. Sanner, S. A. Payne, *Europhys. Lett.* **2012**, *97*, 22002.
[24] W. G. Lawrence, S. Thacker, S. Palamakumbura, K. J. Riley, V. V. Nagarkar, *IEEE Trans. Nucl. Sci.* **2012**, *59*, 215.
[25] E. A. McKigney, R. E. Del Sesto, L. G. Jacobsohn, P. A. Santi, R. E. Muenchausen, K. C. Ott, T. M. McCleskey, B. L. Bennett, J. F. Smith, D. W. Cooke, *Nucl. Instrum. Methods Phys. Res., Sect. A* **2007**, *579*, 15.
[26] R. K. Feller, G. M. Purdy, D. Ortiz-Acosta, S. Stange, A. Li, E. A. McKigney, E. I. Esch, R. E. Muenchausen, R. Gilbertson, M. Bacrania, B. L. Bennett, K. C. Ott, L. Brown, C. S. Macomber, B. L. Scott, R. E. Del Sesto, *J. Mater. Chem.* **2011**, *21*, 5716.
[27] Z. Kang, M. Barta, J. Nadler, B. Wagner, R. Rosson, B. Kahn, *J. Lumin.* **2011**, *131*, 2140.
[28] C. Dujardin, D. Amans, a. Belsky, F. Chaput, G. Ledoux, a. Pillonnet, *IEEE Trans. Nucl. Sci.* **2010**, *57*, 1348.
[29] V. V. Vistovskyy, A. V. Zhyshkovych, O. O. Halyatkin, N. E. Mitina, A. S. Zaichenko, P. A. Rodnyi, A. N. Vasil'ev, A. V. Gektin, A. S. Voloshinovskii, *J. Appl. Phys.* **2014**, *116*, 054308.
[30] Z. Kang, Y. Zhang, H. Menkara, B. K. Wagner, C. J. Summers, W. Lawrence, V. Nagarkar, *Appl. Phys. Lett.* **2011**, *98*, 181914.
[31] G. D. Wilk, R. M. Wallace, J. M. Anthony, *J. Appl. Phys.* **2001**, *89*, 5243.
[32] E. Bersch, S. Rangan, R. Bartynski, E. Garfunkel, E. Vescovo, *Phys. Rev. B* **2008**, *78*, 085114.
[33] A. Callegari, E. Cartier, M. Gribelyuk, H. F. Okorn-Schmidt, T. Zabel, *J. Appl. Phys.* **2001**, *90*, 6466.
[34] C. LeLuyer, M. Villanueva-Ibañez, a. Pillonnet, C. Dujardin, *J. Phys. Chem. A* **2008**, *112*, 10152.
[35] A. Lauria, I. Villa, M. Fasoli, M. Niederberger, A. Vedda, *ACS Nano* **2013**, *7*, 7041.
[36] L. Armelao, C. Eisenmenger-Sittner, M. Groenewolt, S. Gross, C. Sada, U. Schubert, E. Tondello, A. Zattin, *J. Mater. Chem.* **2005**, *15*, 1838.
[37] L. Armelao, H. Bertagnolli, D. Bleiner, M. Groenewolt, S. Gross, V. Krishnan, C. Sada, U. Schubert, E. Tondello, A. Zattin, *Adv. Funct. Mater.* **2007**, *17*, 1671.
[38] N. Pinna, G. Garnweitner, M. Antonietti, M. Niederberger, *Adv. Mater.* **2004**, *16*, 2196.
[39] J. Buha, D. Arčon, M. Niederberger, I. Djerdj, *Phys. Chem. Chem. Phys.* **2010**, *12*, 15537.
[40] J. Tang, J. Fabbri, R. D. Robinson, Y. Zhu, I. P. Herman, M. L. Steigerwald, L. E. Brus, *Chem. Mater.* **2004**, *16*, 1336.
[41] E. Tirosh, G. Markovich, *Adv. Mater.* **2007**, *19*, 2608.
[42] G. I. Britvich, A. I. Peresypkin, V. I. Rykalin, V. G. Vasil'chenko, L. D. Kornylovskaya, S. A. Malinovskaya, V. T. Skripkina, V. M. Shershukov, E. G. Yushko, A. V Kulichenko, A. I. Pyshchev, *Nucl. Instrum. Methods Phys. Res., Sect. A* **1993**, *326*, 483.
[43] P. Sartori, M. Weidenbruch, *Angew. Chem. Int. Ed.* **1964**, *3*, 376.
[44] R. H. Nielsen, *Kirk-Othmer Encycl. Chem. Technol.* **2000**, *4*, 1.
[45] Y. Zhang, X. Sun, R. Si, L. You, C. Yan, *J. Am. Chem. Soc.* **2005**, *127*, 3260.
[46] X. Ye, J. E. Collins, Y. Kang, J. Chen, D. T. N. Chen, A. G. Yodh, C. B. Murray, *Proc. Natl. Acad. Sci. U.S.A.* **2010**, *107*, 22430.
[47] S. Mourdikoudis, L. M. Liz-Marzán, *Chem. Mater.* **2013**, *25*, 1465.
[48] R. J. Young, P. A. Lovell, *Introduction to Polymers*, CRC Press, Boca Raton **2011**.
[49] C. Schöttle, P. Bockstaller, D. Gerthsen, C. Feldmann, *Chem. Commun.* **2014**, *50*, 4547.
[50] S. R. Sandler, K. C. Tsou, *J. Phys. Chem.* **1964**, *68*, 300.
[51] A.-L. Bulin, A. Vasil'ev, A. Belsky, D. Amans, G. Ledoux, C. Dujardin, *Nanoscale* **2015**, *7*, 5744.